Manuscript
Journal of Bionic Engineering
https://doi.org/XXXX

RESEARCH ARTICLE

Journal of Bionic Engineering, Available online 12 July 2025. DOI:10.1007/s42235-025-00746-0

# Self-locking Stability Effect Induced by Downwash Flow of the Flapping Wing Rotor

**Si Chen[1,2,3], Lihua Yuan[1,4], Jiawei Xiang[1*], Yuanyuan He[5*], Peng Zhang[2], Yuanhao Cheng[1], Yinjun Pan[6], Shijun Guo[5], Ye Xie[7], Juan Wang[1,4]**

Received: XX XX 2024 / Revised: XX XX 2024 / Accepted: XX XX 2024 / Published online: XX XX 2024
© Jilin University 2024

**Abstract**
Throughout the previous studies, none of them are involved in analysing the downwash flow effect on the control surface of the Flapping Wing Rotor (FWR). An overset CFD numerical model is built up and validated to study the downwash flow's effect on the stability of the FWR. After simulation, a cone like self-lock region which acts as the critical condition determining the stability of FWR is found. Only when the flow's resultant velocity acting on the control surface lies in the stable region, the FWR can keep stable. The size of the cone like self-lock stable region can be enlarged by increasing the maximum feasible deflection angle constrained by mechanical design or enhancing the equivalent downwash flow velocity. Among all the simulated cases, when $J$ = 2.67 ( $f$ = 5 Hz, $\dot{\psi}$ = 5 r/s), the largest average equivalent downwash flow velocities are found. On the other hand, the recovery torque could be enhanced due to the increase of the arm of the lateral force. According to these simulation results, a 43 g FWR model with two control surfaces and two stabilizers is then designed. A series of flight tests is then conducted to help confirm the conclusion of the mechanism research in this work. Overall, this study points out several strategies to increase the flight stability of the FWR and finally realizes the stable climb flight and mild descent flight of the FWR.

**Keywords** Flapping Wing Rotor, Downwash flow, Self-lock stable region.

✉ Jiawei Xiang
jwxiang@wzu.edu.cn

✉ Yuanyuan He
appleyuanyuan@bit.edu.cn

[1]College of Mechanical and Electrical Engineering, Wenzhou University, Wenzhou 325035, China
[2]Department of Air-drop Testing, AVIC Aerospace Life-Support Industries Ltd., Xiangyang 441000, China
[3]College of Aerospace Engineering, Nanjing University of Aeronautics and Astronautics, Nanjing 210016, China
[4]Wenzhou Key Laboratory of Dynamics and Intelligent Diagnosis-Maintenance of Advanced Equipment, Wenzhou 325035, China
[5]College of Aerospace Engineering, Beijing Institute of Technology, Beijing 100081, China
[6]School of Aerospace, Transport and Manufacturing, Cranfield University, Cranfield, MK43 0AL, UK
[7]Intelligent Robot Research Center, Zhejiang Lab, Hangzhou 310000, China

## 1. Introduction

Over the past two decades, micro biomimetic aircraft have sparked a research boom in the academic field [1–3]. In the early stage, the typical micro aircraft can be mainly divided into three types: the fixed wing[4], rotorcraft [5]and the flapping wing[6, 7]. However, the lift as well as the flight performance of most flapping wing Micro Aerial Vehicles (MAVs) continues to be suboptimal compared to their biological counterparts. To harness the full potential of MAVs, recent studies have shifted their focus toward exploring compound configurations. A representative of compound configurations in MAV named Flapping Wing Rotor (FWR) was proposed about ten years ago. The FWR incorporated the characteristics of the bio-inspired flapping wing into rotorcraft and its conceptual feasibility has been verified in the past few years through several prototypes [8, 9].

Since the birth of FWR, the researches on aerodynamic performance of the FWR have never ceased [10, 11]. For example, Guo et al. [12] designed a piezoelectric-driven FWR prototype and examined its aerodynamic force during hover by using theoretical, numerical, and experimental methods. Zhou et al [13] experimentally studied the effects of kinematic parameters on the average lift for a newly proposed FWR model. Their results indicated that a proper selection of the wing structure, initial angle of attack (10° to 15°), and power input of the FWR can lead to a higher averaged lift production. They also studied the kinematics, deformation, and

Published by Springer. This is the Author Accepted Manuscript issued with: Creative Commons Attribution License (CC:BY 4.0).
The final published version (version of record) is available online at DOI:10.1007/s42235-025-00746-0. Please refer to any applicable publisher terms of use.

aerodynamics of a flexible FWR in hover flight by CFD method [14]. The results show that lift augment, rotating moment enhancement, and power efficiency improvement can be achieved when a wing becomes flexible. Chen et al. [15] studied the effects of bore-hole design on the aerodynamics of a FWR in forward flight by CFD method and found that the FWR with bore-hole design can retain their lift enhancement under certain advance ratios and tilt angles of disk plane. Shao et al [16] studied the influence of wing camber on the aerodynamic performance of FWR based on CFD method. They found that when the maximum camber is less than 0.25c, the increase of lift can be achieved by increasing the maximum camber. Also, more lift is generated when the maximum camber position is closer to the middle position of the mean aerodynamic chord. Chen et al. [17] proposed an effective fluid-structure interaction (FSI) model to calculate the aerodynamic forces and passive twist motion for the FWR. Through simulation, they found that as the flapping frequency increases, the lift efficiency of the FWR with variable twist angle will significantly decrease.

Besides, the application of the downwash flow effect in the MAV system is usually researched. For instance, Shi et al. [18] explored the influences of the downwash flow field on the shape of rice plants. They found that the wind speed at the rice canopy reduced and turbulence intensity of the downwash flow field increased as the MAV flight altitude increased from 2 to 8 m. To study the effect of the downwash flow field on the movement of spray droplets in the air, Tang et al. [19] developed a downwash flow field measurement technique based on the high-speed particle image velocimetry. The results showed that the radial distance of the point at which downwash flow reached the ground was proportional to the hovering height of the helicopter whereas the maximum radial velocity near the ground was inversely proportional to the hovering height.

Despite that the flight stability of the flapping wing has been extensively studied [20, 21], only a few researches focused on the FWR's flight dynamics and stability[22]. Wu et al. [23] conducted the numerical study on the open-loop stability of the FWR based on a 30 g FWR prototype. The results show that the FWR has an unstable oscillatory mode as well as a slow divergence mode. Wang et al. [24] designed an effective control mechanism to achieve the controlled fight of a FWR micro aerial vehicle. Dong et al. [9] designed a flapping rotor aircraft with three wings as well as a PID control mechanism to control the attitude of the micro FWR. To further improve the perception accuracy of FWR's state variables, Dong et al. [25] proposed a cross-fusion scheme to tightly integrate onboard inertial and external visual information and experimentally verified it through two FWR models with different driving and control principles.

Despite the above efforts, none of them are involved in theoretically analysing the downwash flow effect on the control surface of the FWR. The reason for placing the control surfaces below the FWR's body remains unknown. Therefore, this work tries to study the flow mechanism of the downwash flow interacting with the control surface and finds the effect of the downwash flow on the FWR's stability. On the other hand, the effects of the control surface's vertical position, the advance ratio and the deflection angle on the lateral force generation and the FWR's stability are also studied in this work. In this study, to pay more attention to the impact of downwash flow on a single control surface, the control surface is simplified as a rectangle panel.

In this paper, a CFD overset grid model and a lift measurement system are introduced and verified in section 2. Then, in Section 3, the evolution of the downwash vortices around the control surface is analysed detailly. At the same time, the effect of the control surface's vertical position, the advance ratio and the deflection angle on the lateral force generation and the FWR's stability are then investigated. Besides, according to the results based on the mechanism studies, a FWR with two control surfaces and two stabilizers is made. With the help of the control surfaces, the stabilizers and the PID control algorithm, the FWR realizes the stable climb flight. A conclusion of the study is finally drawn in Section 4.

## 2. Numerical Model and Experimental Set Up

### 2.1. CFD Overset Grid Model of the FWR

In this paper, to study the flow mechanism of the downwash flow in generating the lift as well as the lateral forces on the control surface, a CFD overset grid model is built up where the control surface is simplified as a rectangle panel as shown in Fig 1.

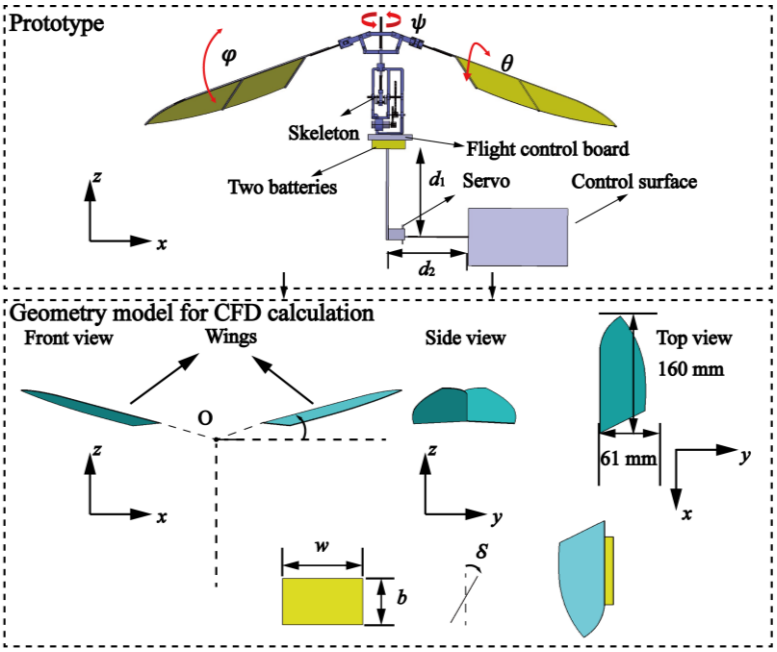


**Fig 1.** Geometry definition of the FWR and its control surface for CFD calculation

As shown in Fig 1, the detailed relative position between the control surface and the wing is given by two parameters ( $d_1$ and $d_2 = 80$ mm). Besides, the size of the single wing is defined as 160mm×61mm. The motion of the FWR could be decomposed into flapping motion ( $\varphi$ ), twist motion ( $\theta$ ) and rotary motion ( $\psi$ ). Meanwhile, the $\delta$ stands for the deflection angle of the control surface.

In this work, the CFD solver used in this paper is fluent 19.0 and the meshing mode of fluent as given in Fig 2. The far field boundary of the whole fluid field and the first level grid refinement region are both defined as the sphere. The outer bound radius of the first level grid refinement region is about 5 times the wing span length while the radius of far field boundary accounts for 15 times the wing span length. The first level grid refinement region includes two overset grid regions and a second level grid refinement region. Wherein, each overset grid region contains one FWR's wing while the second level grid refinement region contains the control surface. A user-defined function is coded in C language to make the overset grid regions rotate about the centre of the whole fluid field. These rotation motions can be decomposed into three mutually orthogonal components to simulate the flapping, twisting and rotary motion of our FWR model. According to the previous studies[26, 27], the *k*-*ω* SST model and 3D RANS Navier-Stokes equations (as defined in Eq.1 and Eq.2) is utilized in the CFD simulation.

$$\nabla \cdot \vec{\boldsymbol{u}} = 0 \tag{1}$$

$$\frac{\partial \vec{u}}{\partial t} + (\vec{\boldsymbol{u}} \cdot \nabla)\vec{\boldsymbol{u}} + \nabla p - \frac{1}{\mathrm{Re}} \nabla^2 \vec{\boldsymbol{u}} = 0 \tag{2}$$

where $\vec{\boldsymbol{u}}$ is the velocity vector and $p$ is the static pressure. Re is the Reynolds Number.

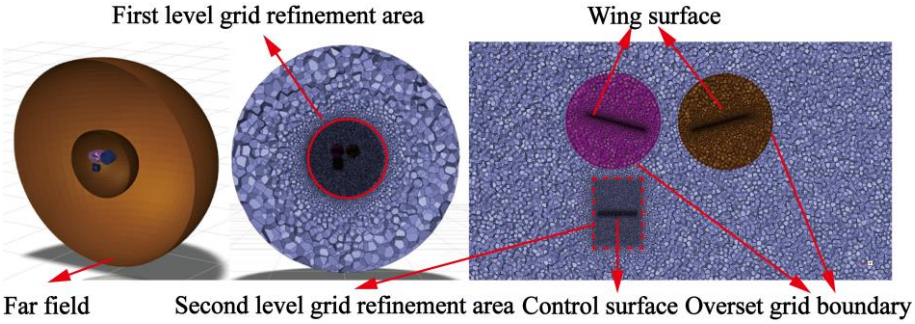


**Fig 2.** Mesh used in the CFD calculation

### 2.2. Force Measurement System for the FWR

As illustrated in Fig 3, the lift measurement system consists of the following components: the FWR, a load cell (YZC-191), a power supply, a signal amplifier, a signal acquisition card (NI USB-6008), a synchronization

circuit and a personal computer. Prior to initiating the force measurement process, it is essential to calibrate the proportional relationship between the pressure exerted on the load cell and the corresponding output voltage. Subsequently, the forces acting on the load cell are converted into a voltage signal, which is recorded by the signal acquisition card in conjunction with the signal amplifier. These voltage signals are then continuously transmitted to the personal computer using LabVIEW software for further analysis.

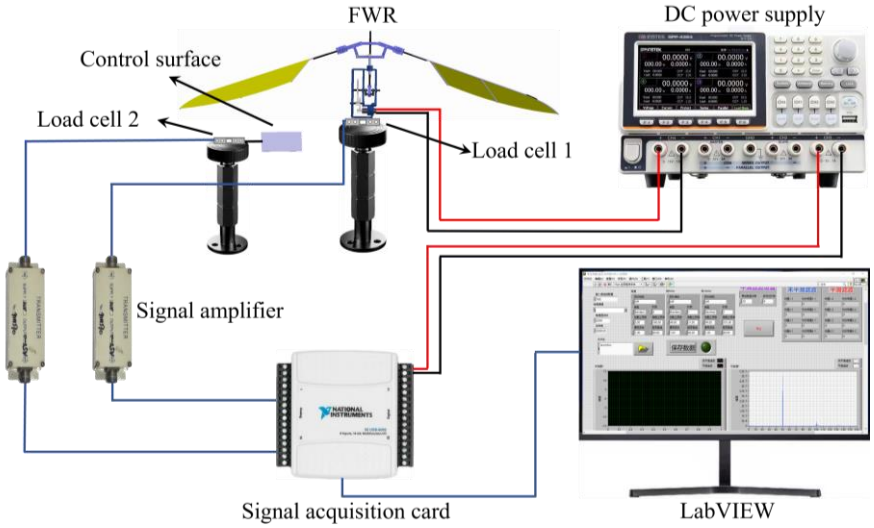


**Fig 3.** Components of the FWR's lift measurement system

On one hand, when testing the lift of the FWR, the differences in the output voltages generated on the load cell 1 during the FWR's flapping process and stationary process correspond to the total forces (a mixture of the inertial and lift forces) acted on the load cell. Once the membrane skin is removed from the wing, the inertial forces can be quantified through the assessment of the load cell voltages. It is imperative that the flapping frequencies of the wing during the measurement of the inertial forces are maintained at the same levels as those employed during the assessment of the total forces. The rotary velocities correspond to horizontal components and exert minimal influence on the vertical inertial forces. If disregarding the variations in twist angles when estimating both inertial and total forces, the net lift forces can be derived by deducting the inertial forces from the aggregate forces. It is anticipated that the average inertial forces over a single flapping cycle will be nearly zero. This methodology has been validated by several previous studies, which underscores its reliability for the force measurement [28, 29].

On the other hand, when testing the lateral force on the control surface, the voltage differences generated on the load cell 2 correspond to the lateral force directly since the control surface stays stationary.

### 2.3. Validation for the CFD Model

To validate the Computational Fluid Dynamics (CFD) model developed in this study, a comparative analysis of a similar FWR case is conducted by comparing the lift and moment results from our CFD simulations with those reported by Wang et al. [30].

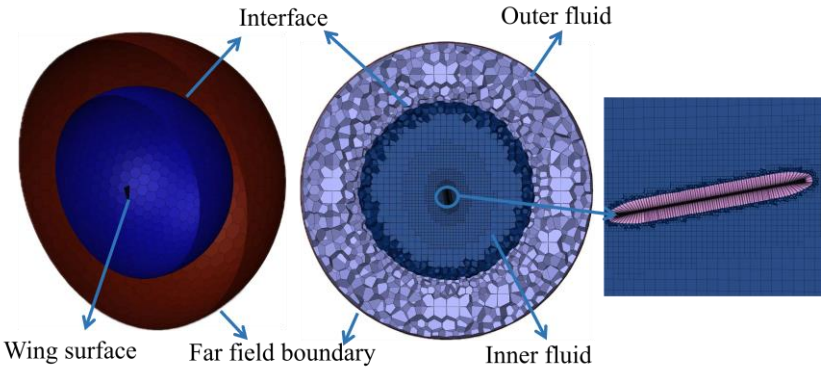


**Fig 4.** Mesh used in the CFD validation case

In this validation scenario, the entire fluid domain is modelled as a sphere, which can be divided into two regions: inner fluid and outer fluid, as illustrated in Fig 4. The variation function of the flapping angle ( $\varphi$ ), twisting angle ( $\theta$ ) and rotary angle ( $\psi$ ) are maintained as described in the existing literature as shown in Fig 5. According to Wang, the shape of the wing is simplified as a flat plane with a relative thickness of 3% and an aspect

ratio of $\lambda = 5$. Additionally, the reference length ($l_{ref}$) and reference velocity ($U_{ref}$) are defined as wing chord $l_{ref} = c$ and the average flapping velocity at the wing tip is given by $U_{ref} = 4c\lambda f\Delta\varphi$. Wherein, the $f$ is short for flapping frequency and $\Delta\varphi$ is the flapping amplitude [30]. Based on these definitions, the lift and rotational moment coefficients $C_L$ and $C_m$ are calculated as follows:

$$C_L = \frac{2L}{\rho(U_{ref})^2 S} \tag{3}$$

$$C_m = \frac{2m_{rotary}}{\rho(U_{ref})^2 Sc} \tag{4}$$

where $L$ and $m_{rotary}$ (rotational moment) are the aerodynamic force and the moment in rotary direction. Besides, $\rho$ denotes the air density. After calculation, the simulation results are plotted in Fig 6.

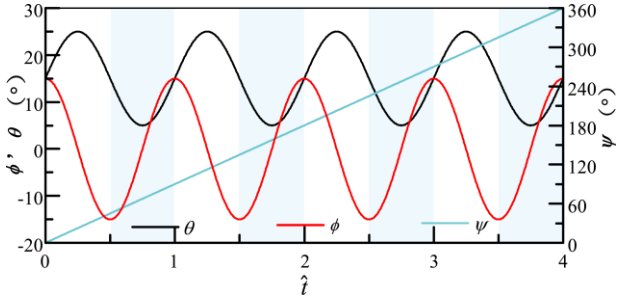


**Fig 5.** Variation of flapping angles, twisting angles and rotary angles in four periods

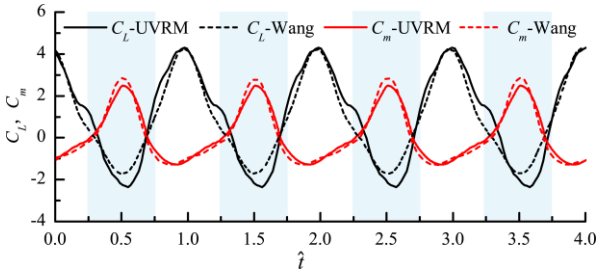


**Fig 6.** Comparison in lift coefficients and rotational moment coefficients between CFD calculation by fluent software and computational results by Wang et al

As illustrated in Fig 6, the trends of the lift coefficient and rotational moment coefficient curves obtained through Fluent software in this study align closely with those reported by Wang et al[30]. According to Wang's results, the average lift coefficients and rotational moment coefficients are $\bar{C}_L = 0.92$ = 0.92 and $\bar{C}_m = 0.13$. In comparison, the $\bar{C}_L$ equals to 0.922 and $\bar{C}_m$ equals to 0.123 in this paper, both of which are in close agreement with Wang et al.'s findings [30].

Besides, a comparison between our experiment results and the simulation results is also made to further prove the accuracy of the CFD model. In this validation case, the position of the control surface is given by $d_1 = 0$ mm and $d_2 = 80$ mm. According to our experiment test, the flapping frequency and the average rotary speed of the FWR are 5 Hz and 20.94 rad/s (3.33 r/s) respectively. That is, in this case, the advance ratio equals to 1.78. Meanwhile, the deflection angle ($\delta$) of the control surface is set as 0°.

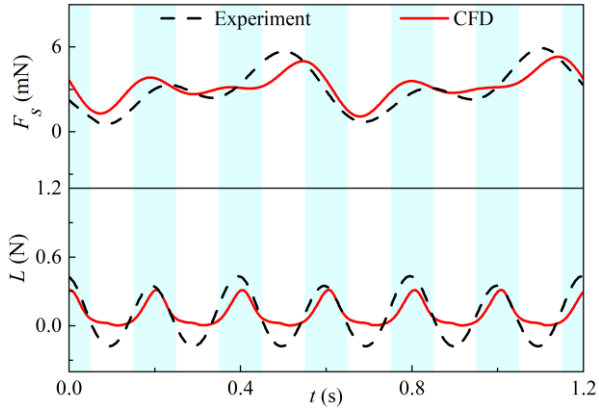


**Fig 7.** Comparison in lift and lateral force on the control surface between the experiment results and the simulation results

After comparison, the curves of the lift and the lateral force on the control surface are plotted in Fig 7. According to Fig 7, the experimental curves and the CFD curves show quite similar trends. The average lifts by the experiment and the CFD are 0.095 N and 0.107 N respectively. Also, the average lateral forces by the experiment and the CFD are 0.0031 N and 0.0028 N respectively. The differences in the peak values and the timing of when the peaks are reached between experiment and simulation should come from the deformation of the FWR's wings and control surfaces.

Above all, the two comparison cases indicate that the CFD model employed in this research is well-suited for aerodynamic studies of the FWR.

## 3. Results and Discussion

### 3.1. The Kinematic Parameters in the Test Cases

To separate the contributions of individual variables to lateral force and stability, 9 case sets (from case set 1 to case set 9) were listed in Table. 1 to study the effect of the control surface's vertical position, the advance ratio and the deflection angle on the lateral force generation and the FWR's stability. Meanwhile, the flow mechanism of the downwash flow is also studied wherein the $d_2$ is given as 80 mm for all cases. The rotary speeds ($\dot{\psi}$) in all these 36 cases keep the same as 5 r/s wherein the positive direction is defined in the Fig 1. The definition of the advance ratio (the ratio of the forward flight velocity to the flapping

velocity at the plate tip) can be found in the previous paper [30].

**Table. 1** Input parameters for the simulation cases

| Case No. | $f$ (Hz) | $\delta$ (°) | $d_1$ (mm) | $J$ | Case No. | $f$ (Hz) | $\delta$ (°) | $d_1$ (mm) | $J$ |
|---|---|---|---|---|---|---|---|---|---|
| 1-1 | 2.5 | -30° | 80 | 5.34 | 2-1 | 2.5 | 0° | 80 | 5.34 |
| 1-2 | 5 | -30° | 80 | 2.67 | 2-2 | 5 | 0° | 80 | 2.67 |
| 1-3 | 10 | -30° | 80 | 1.33 | 2-3 | 10 | 0° | 80 | 1.33 |
| 1-4 | 15 | -30° | 80 | 0.89 | 2-4 | 15 | 0° | 80 | 0.89 |
| 3-1 | 2.5 | 30° | 80 | 5.34 | 4-1 | 2.5 | -30° | 40 | 5.34 |
| 3-2 | 5 | 30° | 80 | 2.67 | 4-2 | 5 | -30° | 40 | 2.67 |
| 3-3 | 10 | 30° | 80 | 1.33 | 4-3 | 10 | -30° | 40 | 1.33 |
| 3-4 | 15 | 30° | 80 | 0.89 | 4-4 | 15 | -30° | 40 | 0.89 |
| 5-1 | 2.5 | 0° | 40 | 5.34 | 6-1 | 2.5 | 30° | 40 | 5.34 |
| 5-2 | 5 | 0° | 40 | 2.67 | 6-2 | 5 | 30° | 40 | 2.67 |
| 5-3 | 10 | 0° | 40 | 1.33 | 6-3 | 10 | 30° | 40 | 1.33 |
| 5-4 | 15 | 0° | 40 | 0.89 | 6-4 | 15 | 30° | 40 | 0.89 |
| 7-1 | 2.5 | -30° | 0 | 5.34 | 8-1 | 2.5 | 0° | 0 | 5.34 |
| 7-2 | 5 | -30° | 0 | 2.67 | 8-2 | 5 | 0° | 0 | 2.67 |
| 7-3 | 10 | -30° | 0 | 1.33 | 8-3 | 10 | 0° | 0 | 1.33 |
| 7-4 | 15 | -30° | 0 | 0.89 | 8-4 | 15 | 0° | 0 | 0.89 |
| 9-1 | 2.5 | 30° | 0 | 5.34 | | | | | |
| 9-2 | 5 | 30° | 0 | 2.67 | | | | | |
| 9-3 | 10 | 30° | 0 | 1.33 | | | | | |
| 9-4 | 15 | 30° | 0 | 0.89 | | | | | |

### 3.2. Flow Mechanism of the Downwash Flow

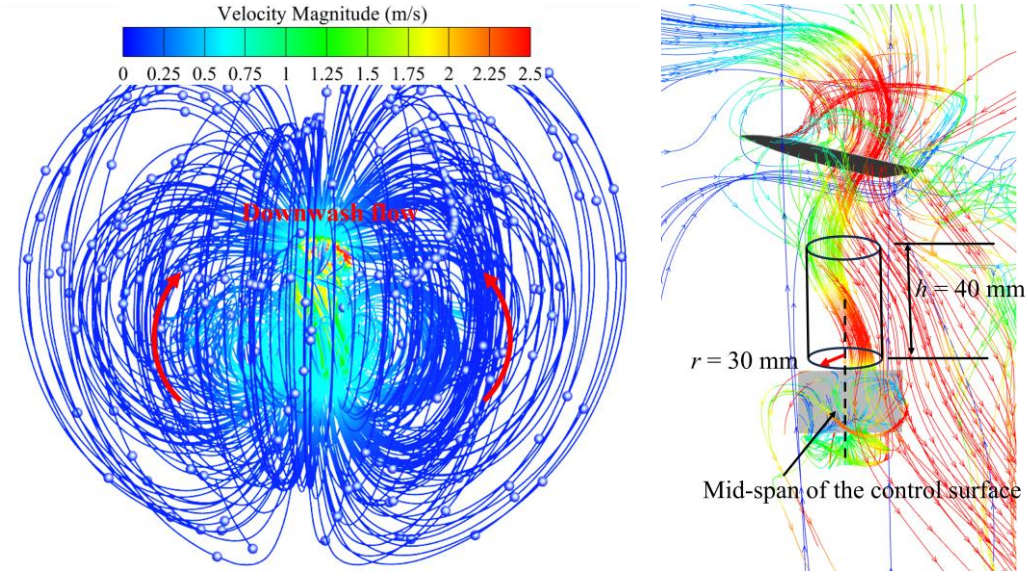


**Fig 8.** The downwash flow of the whole fluid field (the video is submitted as the attachment)

According to Fig 8, upon the FWR works, the downwash flow would interact with the control surface ( $d_3 = 20$ mm). It is found that apparent downwash flow caused by the FWR's wing would collide with the control surface and then continue moving along nearly -$z$ direction.

Also, it is found that the flow-field morphology across different control surface's vertical positions ( $d_1$ ) shares a similar trend. To avoid repetition, Fig 9 gives the velocity magnitude terms within the fluid field around the FWR by focusing all the cases from case 1 to case 3 ( $d_1 = 80$ mm). Wherein, the LE is short for the leading edge while the TE stands for the trailing edge. The time $\hat{t} = 0$ corresponds to the mid-downstroke timing for the FWR's wings. Besides, it is observed that the flow field shows a periodic variation pattern wherein the variation period is 0.2 s. This is because that both the flapping period and rotary period

equal to 0.2 s. Then, the minimum common multiple period corresponds to the flapping period and rotary period is 0.2 s.

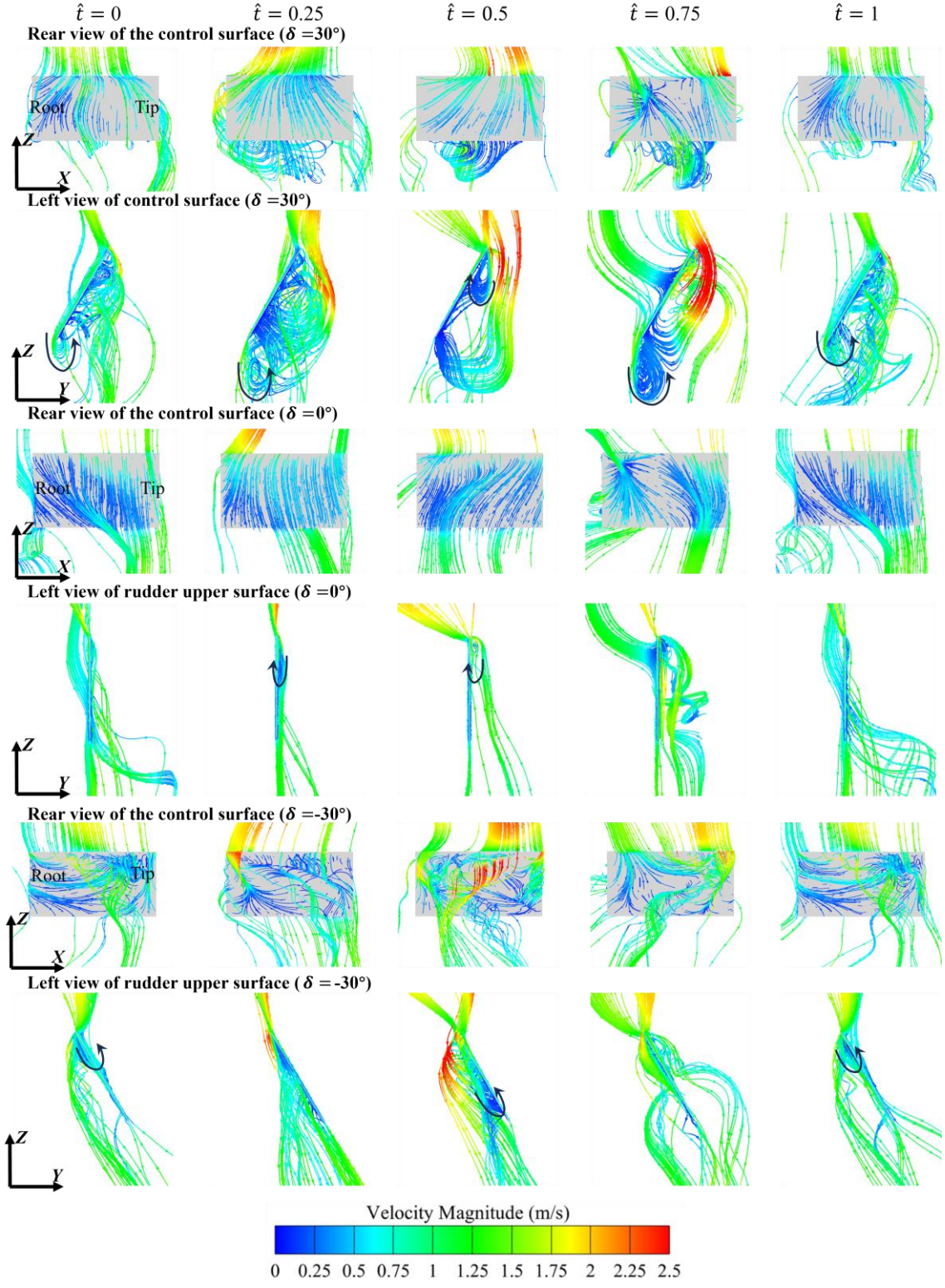


**Fig 9.** Velocity distribution of FWR in a lateral force cycle across different deflection angle ( $f = 5$ Hz, $J = 2.67$, $d_1 = 80$ mm)

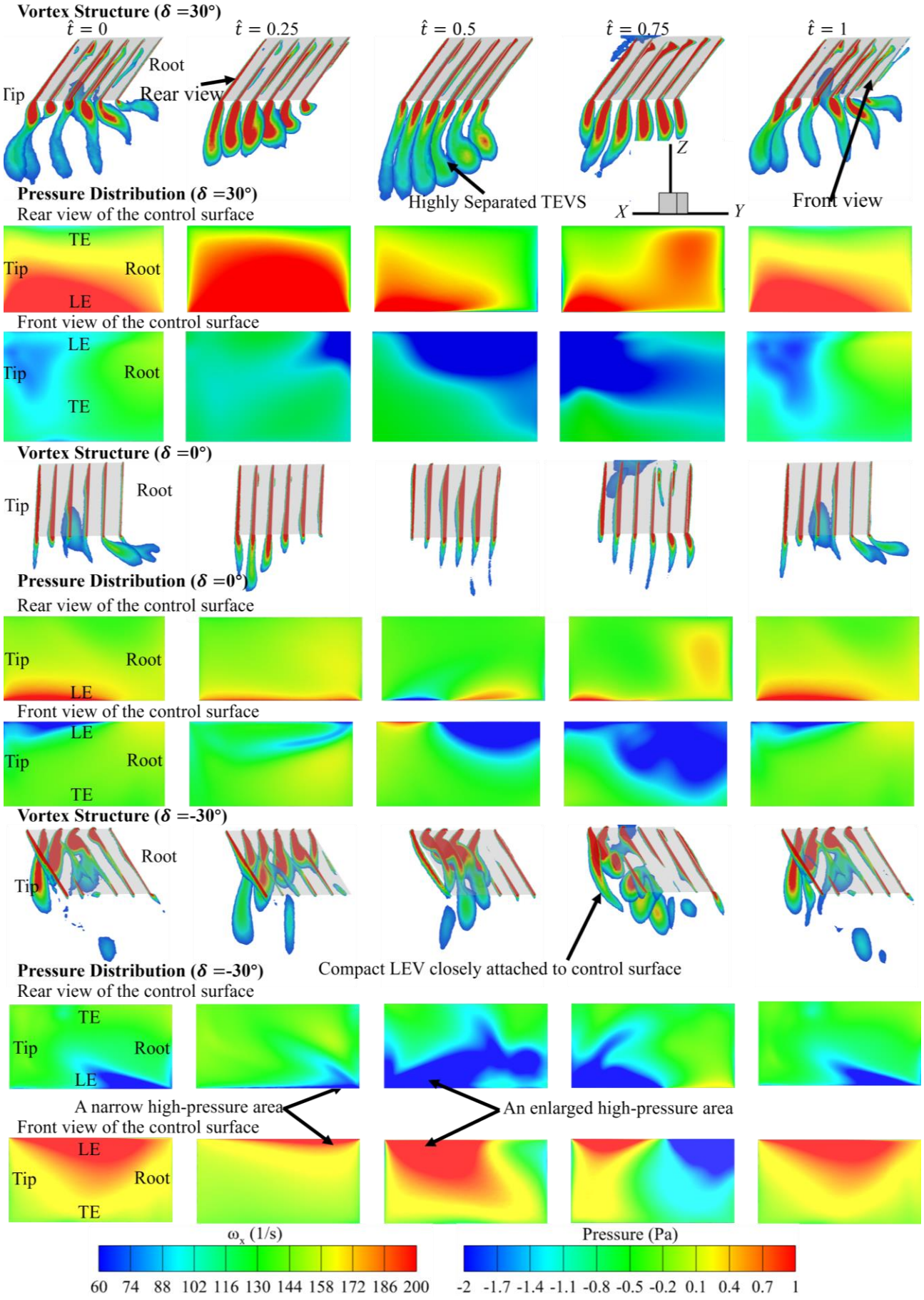


**Fig 10.** Flow patterns and pressure distribution of FWR in a lateral force cycle across different deflection angles ( $f = 5$ Hz, $J = 2.67$, $d_1 = 80$ mm)

According to the Fig 9, the largest velocity appears near the leading edge. The downwash flow does not show the symmetric form about $x$ axis between the two cases with $\delta = 30°$ and $\delta = -30°$. In the $\delta = 30°$ case, the downwash flow continues detaching from the control surface throughout the single period. However, the separation degree of the downwash flow is weaker in the $\delta = -30°$ case. It means the neutral deflection angle which can generate zero lateral force should be a negative value.

According to the Fig 10, if focusing on the spanwise vorticity, it is observed that despite the large spanwise vorticity areas are found around the leading edge when the $\delta = -30°$, the dominant spanwise vorticity areas are found to be around the trailing edge when the $\delta = 30°$ and $\delta = 0°$. The downwash flow does not evolve purely in the -z direction when $\delta = 0°$. Instead, a small +y direction downwash flow leads to the fact that the trailing-vortices grow on the front side of the control surface as shown in Fig 10. When it comes to the pressure distribution, it appears that the largest positive/negative pressure areas mainly occur around the leading-edge of the control surface. Besides, the negative pressure appears on the side where a bunch of vortices accumulate.

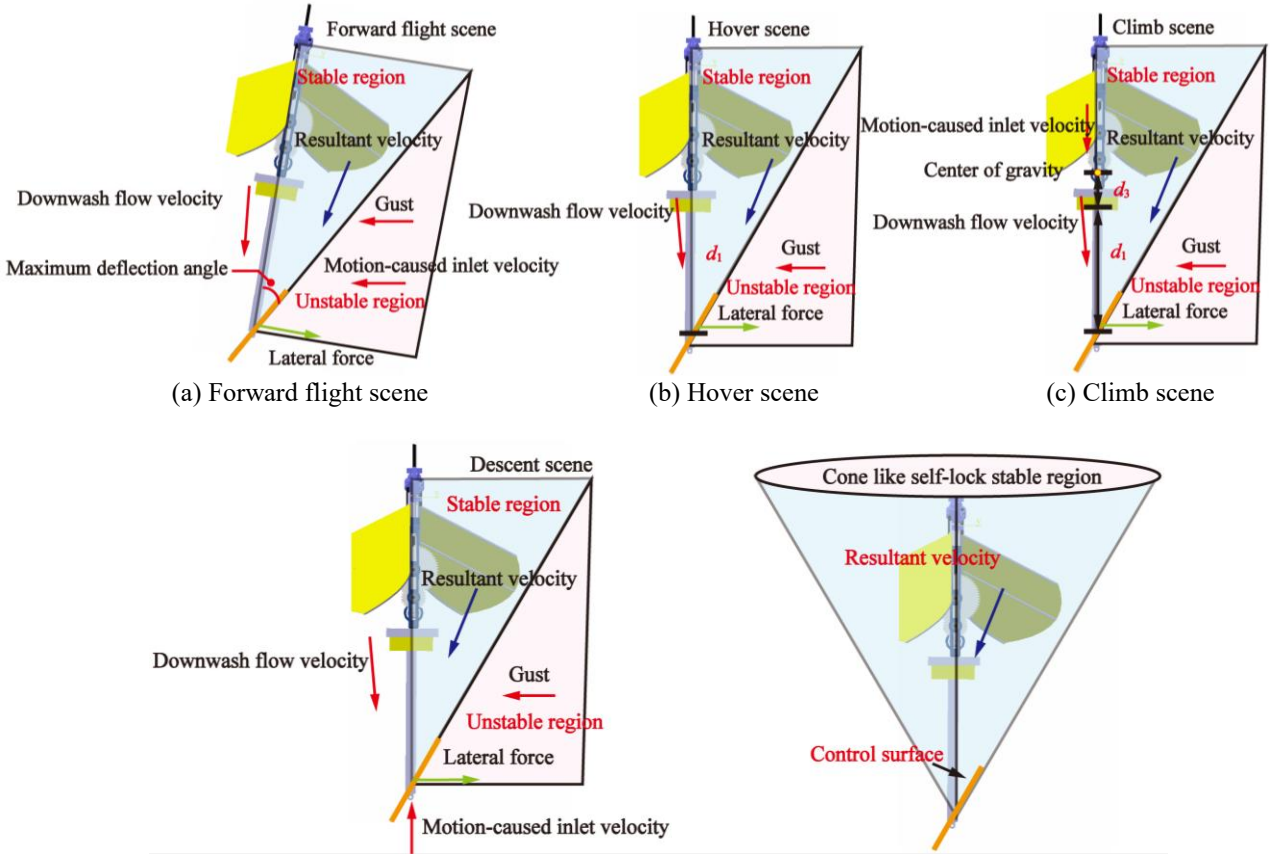


(a) Forward flight scene (b) Hover scene (c) Climb scene

(d) Descent scene (e) Cone like self-lock region

**Fig 11.** Schematic diagram of self-locking phenomenon induced by the downwash flow

From the above the results, it is known that the downwash flow would interact with the control surface and cause the vortices' evolution process around the control surface. Thus, a lateral force or a control torque is generated. If turning the control surface to its maximum feasible deflection angle constrained by the mechanical design and performing a simplified force analysis, the control surface's contribution to the FWR's stability could be simply observed. According to the Fig 11 (a) and Fig 11 (b), if without the gust or the horizontal flight velocity, the control surface downwash effect would help stabilize the FWR during its hovering flight or forward flight with a small inclination angle since the lateral force can generate an attitude recovery torque to stop the FWR from rollover. However, if the resultant velocity vector composed of the equivalent downwash velocity, horizontal flight velocity and gust velocity exceeds the blue region (as marked in the Fig 11), the lateral force on the control surface would flip its direction and intensify the rollover of the FWR. Apparently, this kind of situation is not desirable. As shown in Fig 11 (c), the incoming flow velocity caused by the climb velocity can facilitate the stability of the FWR. Moreover, the descent process of the FWR is the situation that is most prone to rollover. Even without the gust or horizontal flight velocity, the rollover of the FWR could happen when the descent velocity is larger than the equivalent downwash flow velocity as shown in Fig 11 (d).

Above all, only when the resultant velocity lies in the stable region, the FWR can keep stable. This phenomenon

is somewhat like the self-lock phenomenon in tribology. Also, since the rollover could happen in any direction (0°~360°), the self-lock stable region (defined as the region where the FWR can keep stable if the resultant velocity lies in) is a cone like region as shown in Fig 11 (e). The size of the cone like self-lock stable region is mainly affected by the maximum feasible deflection angle constrained by mechanical design and the equivalent downwash flow velocity. Apparently, it is better to enlarge the maximum feasible deflection angle and the equivalent downwash flow velocity to make the stable region larger. Thus, in the following stage, the equivalent downwash flow velocity in different cases is discussed in detail.

According to Fig 9, before the downwash flow collides with the control surface, the downwash flow is almost evenly distributed. Thus, in this study, the equivalent downwash flow velocity is defined as the average downwash flow velocity within a cylindrical region above the control surface as shown in Fig 8.Wherein, the cylindrical starts from the upper edge of the control surface when the deflection angle equals to 0°. The centre of the cylindrical is at the mid-span of the control surface and the radius of the cylindrical equals to 30 mm. Besides, the height of the cylindrical is 40 mm and the average downwash flow velocity is sampled at the mid downstroke time. According to Fig 12, under any advance ratio and deflection angle, the average equivalent downwash flow velocity decreases with the increase of the vertical distance. When $J$ = 2.67 ( $f$ = 5 Hz, $\dot{\psi}$ = 5 r/s), the largest average equivalent downwash flow velocities are found.

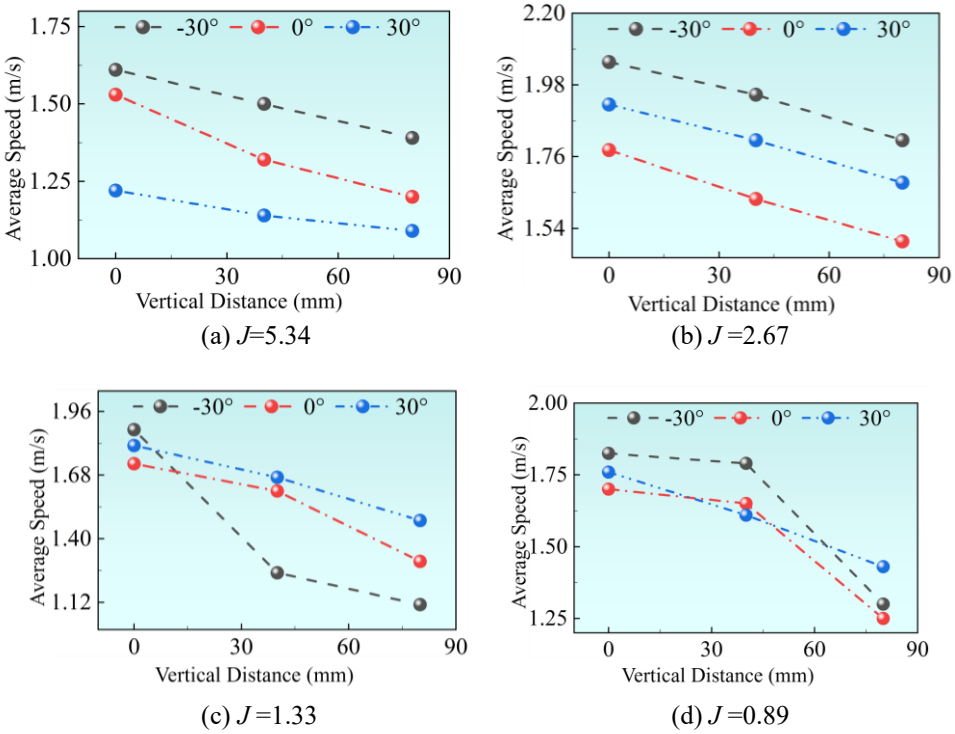


(a) $J$=5.34 (b) $J$ =2.67

(c) $J$ =1.33 (d) $J$ =0.89

**Fig 12 .** Average equivalent downwash flow velocity in -z direction within the specific cross-section

### 3.3. Lateral Forces on the Control Surface and Lift

Apart from guaranteeing enough average equivalent downwash flow velocity, it is also important to enlarge the lateral forces on the control surface as well as the attitude recovery torque. As shown in Fig 13, the periods of the lateral force curves are the minimum common multiple periods corresponding to the flapping period and rotary period. As shown in Fig 13 (a)-Fig 13 (c), given the same advance ratio and different deflection angle (from -30° to 30°), the lateral force curves show a similar variation trend. Within the single variation period, the largest variation amplitude is found when the advance ratio equals to 1.33. Also, upon the unsmooth rotary motion occurs (which may be caused by the bearing jamming and the advance ratio reaches 0.89), the lateral force would oscillate around zero and almost no net lateral force is generated. If taking a glance at the lift, it is found that the period of the lift curves equal to the flapping period of the FWR's wings. With the increase of the flapping frequency, the peak lift increases dramatically while the variation of the deflection angle does not affect the lift generation.

When it comes to the average lateral force in each case, it is found that the average lateral force increases with both the deflection angle as well as the advance ratio as shown in Fig 14. Meanwhile, if reducing the vertical distance ( $d_1$ ) from 80 mm to 0 mm, the lateral forces show a slightly increasing trend. However, in that case, the arm of the lateral force nearly reduces by a factor of 10 (from $d_1 + d_3$

to $d_3$, $d_3 = 9$ mm), which leads to an apparent reduction of the attitude recovery torque. Thus, according to Fig 14, the attitude recovery torque should eventually increase with the increase of the vertical distance.

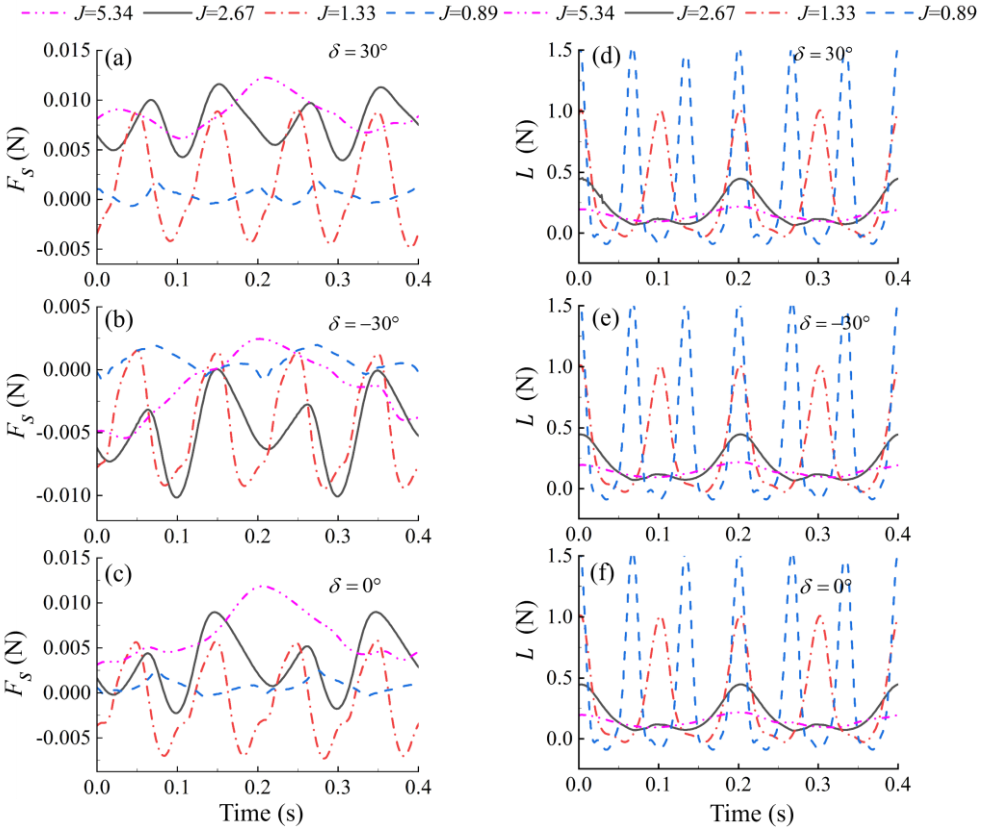


**Fig 13.** Lateral force and lift curves within 0.4 s under different flapping frequencies and deflection angle ( $d_1 = 80$ mm)

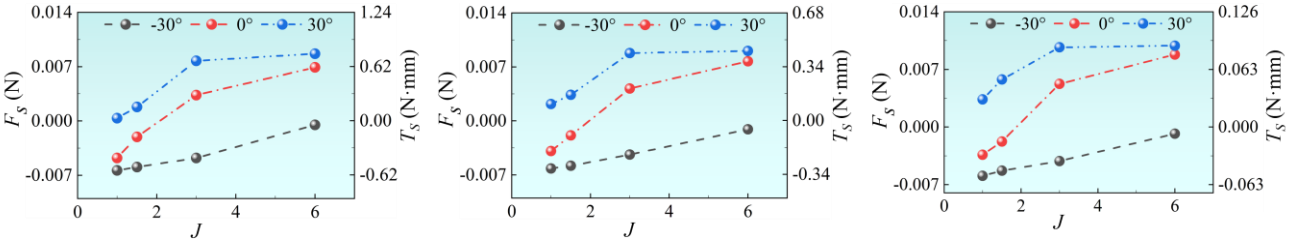


(a) $d_1 = 80$ mm; (b) $d_1 = 40$ mm; (c) $d_1 = 0$ mm

**Fig 14.** Average lateral force

### 3.4. Controlled Flight Test

According to the analysis in the previous sections, it is better to increase the distance between the control surface and the FWR body to gain larger lateral forces' arm. Also, the downwash flow velocity decreases with the increase of the gap between the control surface and the FWR body. Thus, according to these results, a FWR model is made as shown in Fig 15. The 43 g FWR prototype consists of two orthogonal control surfaces and two stabilizers with large height which can not only guarantee the large lateral forces' arm but also ensure the downwash flow velocity acting on the control surface becomes too small. Then, a control board integrated with an in-house PCB board and an ESP32-s3-tiny core is mounted on the FWR to receive the control signal sent from the computer. Wherein, the control signals are transmitted through Wi-Fi. The PID control strategy (defined in the Eq. 3 and Eq. 4) is applied to adjust the deflection angle of the control surfaces as shown in Fig 15. The $\delta_\theta$ is the deflection angles of the control surfaces in the pitch direction of the FWR as marked in the Fig 15 while the $\delta_\varphi$ is the deflection angles of the control surfaces in the roll direction of the FWR. The $\theta_B(t)$ is the pitch angle of the FWR as given in the Fig 15 while the $\varphi_B$ is the roll angle of the FWR. After

our amounts of trials, the P, I and D values are given as 0.28, 0 and 0.02 respectively.

$$\delta_\theta = P\times\theta_B(t) + I\times\sum_{i=0}^{t}\theta_B(i) + D\times(\theta_B(t)-\theta_B(t-1)) \quad (3)$$

$$\delta_\varphi = P\times\varphi_B(t) + I\times\sum_{i=0}^{t}\varphi_B(i) + D\times(\varphi_B(t)-\varphi_B(t-1)) \quad (4)$$

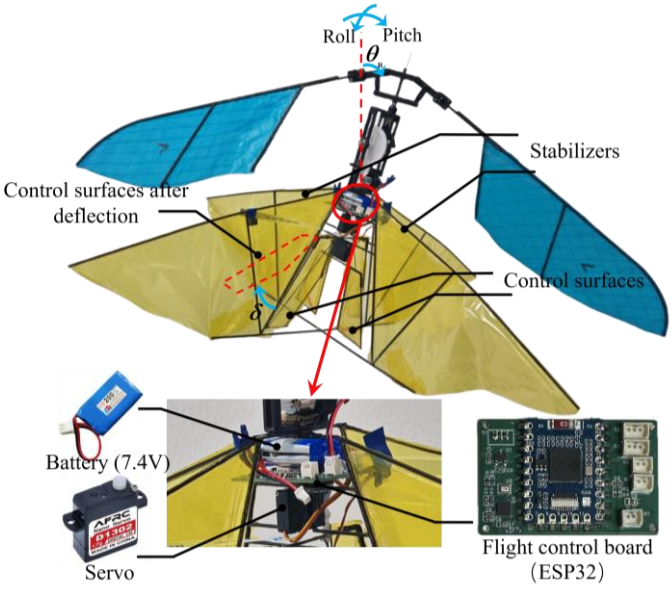


**Fig 15.** FWR prototype

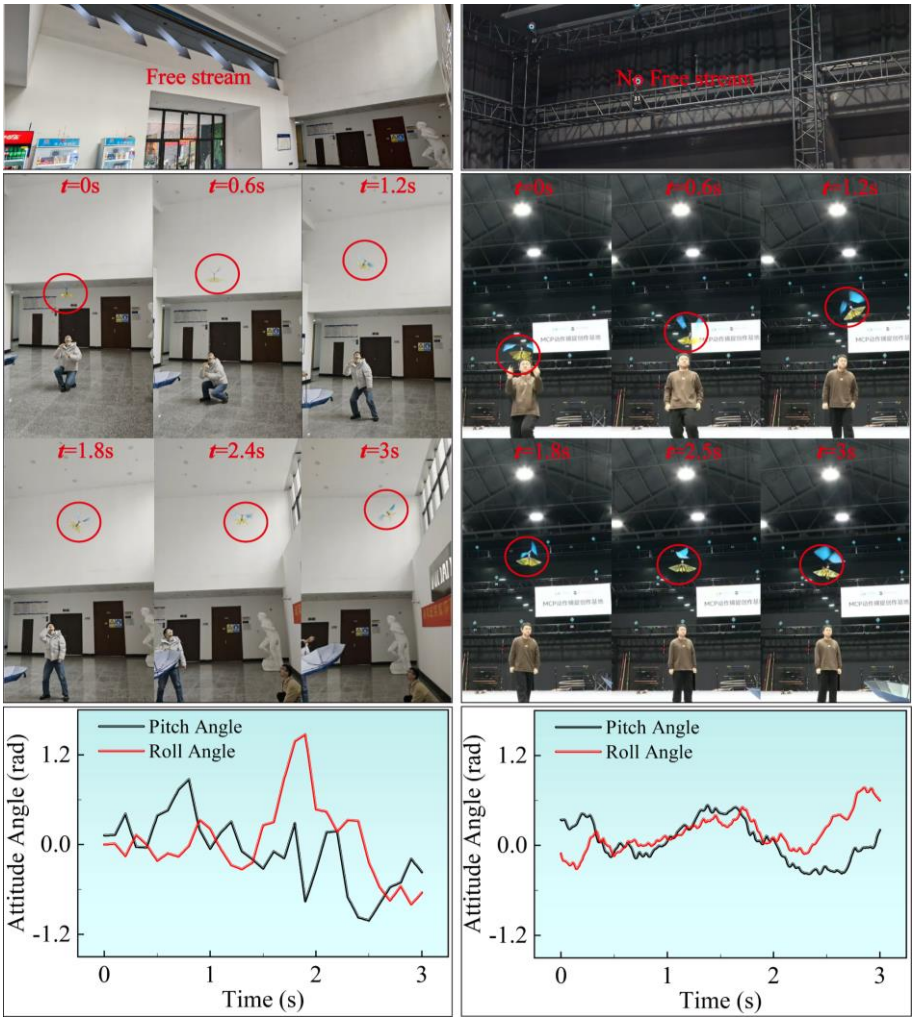


**Fig 16.** Indoor stable flight tests (the videos are submitted as the attachment)

Then, a series of indoor flight tests were conducted. Wherein, 5 flight test videos under no freestream and 5 flight test videos under certain freestream are submitted as attachments. By randomly choosing one freestream case and one no freestream case, the video snapshots and the corresponding attitude angle curves are plotted in Fig 16. The motor's power is adjusted through the PWM controller integrated into the control board. Although the rated voltage of the battery is 7.4 V, the real voltage of the battery can reach 8.4 V in its full charge state. Thus, when the preset PWM value ranges from 0 to 1023, the input voltage for the motor changes from 0 V to 8.4 V. From Fig 16, it is observed that the FWR can rise stably and its roll angles as well as the pitch angles are limited to no more than 35° during most of the flight time under the no freestream case. Also, even with certain indoor freestreams, the FWR can still sustain stability. Despite the FWR's maximum roll angles can reach around 70° during the flight process, the FWR can realize the attitude recovery. It should be because the downwash flow acting on the control surfaces greatly helps to keep the stability of the FWR.

**Fig 17.** Outdoor flight test (the video is submitted as the attachment)

Besides, an outdoor flight test was conducted as shown in Fig 17, the in-house FWR climbed stably and it reached the 4th floor of the college building in just 6 seconds (PWM value equals to 900). But when we reduce the input voltage to stop the FWR from disappearing from our sight and make it execute the fast-landing mission (PWM value equals to 0), the FWR cannot sustain its attitude and turn over in the following 2 seconds. This instability comes from the fast descent velocity which causes the flow's resultant velocity to enter the unstable region for the FWR. Above all, the phenomenon in Fig 16 and Fig 17 assist in confirming the conclusion of the mechanism research in this work.

## 4. Conclusion

In this paper, an overset CFD numerical model and a lift measurement system are built up. Wherein, the CFD model is validated by comparing the simulated results with those obtained by the lateral force measurement experiments. The evolution of the downwash vortices around the control surface is then analysed in detail. Meanwhile, the effect of the control surface's vertical position, the advance ratio and the deflection angle on the lateral force generation and the FWR's stability are then investigated. From the numerical study, the following key conclusions are drawn:

The downwash flow does not show the symmetric form about $x$ axis between the two cases with $\delta = 30°$ and $\delta = -30°$. It means the neutral deflection angle which can generate zero lateral force should be a negative value. When it comes to the pressure distribution, it appears that the largest positive/negative pressure areas mainly occur

around the leading-edge of the control surface. Besides, the negative pressure appears on the side where a bunch of vortices accumulate.

The downwash flow velocity facilitates the stability of the FWR and leads to a cone like self-lock region. Only when the resultant velocity lies in the stable region, the FWR can keep stable. The size of the cone like self-lock stable region can be enlarged by increasing the maximum feasible deflection angle constrained by mechanical design or enhancing the equivalent downwash flow velocity. When $J$ = 2.67 ( $f = 5$ Hz, $\dot{\psi} = 5$ r/s), the largest average equivalent downwash flow velocities are found. The attitude recovery torque should eventually increase with the increase of the vertical distance.

A 43 g FWR model is designed and three controlled flight tests were conducted. Wherein, a series of indoor flight tests shows that the FWR can be quite stable during the rise flight. It should be because the downwash flow acting on the control surfaces greatly helps to keep the stability of the FWR. The outdoor flight test shows that the large descent velocity can cause the instability of the FWR. These phenomena assist in confirming the conclusion of the mechanism research in this work.

Overall, this study points out several strategies to increase the flight stability of the FWR and finally realizes the stable climb flight and mild descent flight of the FWR.

**Acknowledgments** This work is supported by the following funding organizations in China**:** National Natural Science Foundation of China (Grant No. 52375116 and Grant No. 52105285); the Aeronautical Science Foundation of China (Grant No. ASFC-20230023052001); China Postdoctoral Science Foundation (Grant No. 2024M754237); National Key Research and Development Program of China (2024YFB470920001); Science and Technology Plan Project of Wenzhou Municipality (Grant No. ZG2024001); Basic Public Welfare Research Program of Wenzhou (Grant No. G2023046). (Corresponding author: Jiawei Xiang, Yuanyuan He)

**Data Availability** The datasets generated during the current study are available from the corresponding author on reasonable request.

## Declarations

**Conflict of Interest** The authors declare no competing financial inter est.

## References

1. Fuller, S., Yu, Z., & Talwekar, Y.P. (2022) A gyroscope-free visual-inertial flight control and wind sensing system for 10-mg robots. *Science Robotics*. 7, eabq8184. https://doi.org/10.1126/scirobotics.abq8184
2. Phan, H.V., &Park, H.C. (2020) Mechanisms of collision recovery in flying beetles and flapping-wing robots. *Science*. 370, 1214–1219. https://doi.org/10.1126/science.abd3285
3. Jafferis, N.T., Helbling, E.F., Karpelson, M., &Wood, R. J. (2019) Untethered flight of an insect-sized flapping-wing microscale aerial vehicle. *Nature*. 570, 491–495. https://doi.org/10.1038/s41586-019-1322-0
4. Combes, T.P., Malik, A.S., Bramesfeld, G., & McQuilling, M.W. (2015) Efficient fluid-structure interaction method for conceptual design of flexible, fixed-wing micro-air-vehicle wings. *AIAA Journal*. 53(6), 1442–1454. https://doi.org/10.2514/1.J053125
5. Ramasamy, M., Lee, T.E., & Leishman, J.G. (2007) Flow-field of a rotating-wing micro air vehicle. *Journal of Aircraft*. 44(4), 1236–1244. https://doi.org/10.2514/1.26415
6. Helps, T., Romero, C., Taghavi, M., Conn, A.T., & Rossiter, J. (2022) Liquid-amplified zipping actuators for micro-air vehicles with transmission-free flapping. *Science Robotics*. 7, eabi8189. https://doi.org/10.1126/scirobotics.abi8189
7. Chin, Y.-W., Kok, J.M., Zhu, Y.-Q., Chan, W.-L., Chahl, J.S., Khoo, B.C., & Lau, G.-K. (2020) Efficient flapping wing drone arrests high-speed flight using post-stall soaring. *Science Robotics*. 5, eaba2386. https://doi.org/10.1126/scirobotics.aba2386
8. Dong, X., Li, D., Xiang, J., & Wang, Z. (2020) Design and experimental study of a new flapping wing rotor micro aerial vehicle. *Chinese Journal of Aeronautics*. 33, 3092–3099. https://doi.org/10.1016/j.cja.2020.04.024
9. Chen, S., Wang, L., He, Y., Tong, M., Pan, Y., Ji, B., & Guo, S. (2022) Aerodynamic performance of a flyable flapping wing rotor with passive pitching angle variation. *IEEE Transactions on Industrial Electronics*. 69, 9176–9184. https://doi.org/10.1109/TIE.2021.3112964
10. Wu, J., Yan, H., Zhou, C., & Zhang, Y. (2021) Unsteady aerodynamics of a micro flapping rotary wing in forward flight. *Aerospace Science and Technology*. 111, 106530. https://doi.org/10.1016/j.ast.2021.106530
11. Chen, L., & Zhou, C. (2021) Linearized aerodynamic modelling of flapping rotary wings by rotating the leading-edge suction. *AIAA Journal*. 59, 1–7. https://doi.org/10.2514/1.J060230
12. Guo, S., Li, D., & Wu, J. (2012) Theoretical and experimental study of a piezoelectric flapping wing rotor for micro aerial vehicle. *Aerospace Science and Technology*. 23, 429–438. https://doi.org/10.1016/j.ast.2011.10.002
13. Zhou, C., Wu, J.H., & Guo, S. (2013) Experimental study of a mechanical flapping rotary wing model. *Applied Mechanics and Materials*. 390, 23–27. https://doi.org/10.4028/www.scientific.net/AMM.390.23
14. Zhou, C., & Wu, J. (2021) Kinematics, deformation, and aerodynamics of a flexible flapping rotary wing in hovering flight. *Journal of Bionic Engineering*. 18, 197–209. https://doi.org/10.1007/s42235-021-0014-2
15. Chen, L., Zhou, Y., Zhou, C., & Wu, J. (2022) Effects of bore-hole design on the aerodynamics of a flapping rotary wing in forward flight. *Aerospace Science and Technology*. 127, 107671. https://doi.org/10.1016/j.ast.2022.107671
16. Shao, H., Li, D., Kan, Z., Li, H., Yuan, D., & Xiang, J. (2021) Influence of wing camber on aerodynamic performance of flapping wing rotor. *Aerospace Science and Technology*. 113, 106732. https://doi.org/10.1016/j.ast.2021.106732
17. Chen, L., Wang, L., &Wang, Y.Q. (2022) Efficient fluid-structure interaction model for twistable flapping rotary wings. *AIAA Journal*. 60, 6665–6679. https://doi.org/10.2514/1.J061940
18. Shi, Q., Liu, D., Mao, H., Shen, B., & Li, M. (2021) Wind-induced response of rice under the action of the downwash flow field of a multi-rotor UAV. *Biosystems Engineering*. 203, 60–69. https://doi.org/10.1016/j.biosystemseng.2020.12.012
19. Tang, Q., Zhang, R., Chen, L., Xu, G., Deng, W., Ding, C., Xu, M., Yi, T., Wen, Y., & Li, L. (2020) High-accuracy, high-resolution downwash flow field measurements of an unmanned helicopter for precision agriculture. *Computers and Electronics in Agriculture*. 173, 105390. https://doi.org/10.1016/j.compag.2020.105390
20. Au, L.T.K., & Park, H.C. (2020) Influence of center of gravity location on flight dynamic stability in a hovering tailless FW-MAV: lateral motion. *Journal of Bionic Engine*

*ering*. 17, 148–160. https://doi.org/10.1007/s42235-020-0012-9

21. Taha, H.E., Tahmasian, S., Woolsey, C.A., Nayfeh, A.H., & Hajj, M.R. (2015) The need for higher-order averaging in the stability analysis of hovering, flapping-wing flight. *Bioinspiration & Biomimetics*. 10, 016002. https://doi.org/10.1088/1748-3190/10/1/016002
22. Chen, L., Cheng, C., Zhou, C., Zhang, Y., & Wu, J. (2024) Flapping rotary wing: A novel low-Reynolds number layout merging bionic features into micro rotors. *Progress in Aerospace Sciences*. 146, 100984. https://doi.org/10.1016/j.paerosci.2024.100984
23. Wu, J., Wu, X., Tang, P., Zhang, Y., & Zhou, C. (2023) Dynamic flight stability of a hovering flapping-rotary-wing vehicle. *AIAA Journal*. 1–14. https://doi.org/10.2514/1.J063055
24. Wang, Z., Dong, X., Xiang, J., Li, D., & Tu, Z. (2022) Experimental validation of an effective control mechanism to enable flapping wing rotor stable flight. *Guidance, Navigation and Control*. 2,2250014. https://doi.org/10.1142/S2737480722500145
25. Dong, X., Wang, Z., Liu, F., Li, S., Fei, F., Li, D., & Tu, Z. (2022) Visual-inertial cross fusion: a fast and accurate state estimation framework for micro flapping wing rotors. *Drones*. 6, 1–18. https://doi.org/10.3390/drones6040090
26. Liu, L., Li, H., Ang, H., & Xiao, T. (2018) Numerical investigation of flexible flapping wings using computational fluid dynamics/computational structural dynamics method. *Proceedings of the Institution of Mechanical Engineers, Part G: Journal of Aerospace Engineering*. 232, 85–95. https://doi.org/10.1177/0954410016671343
27. Hao, J., Wu, J., & Zhang, Y. (2019) Aerodynamic performance of a passive pitching model on bionic flapping wing micro air vehicles. *Applied Bionics and Biomechanics*. 10, 1504310. https://doi.org/10.1155/2019/1504310
28. Chen, S., Wang, L., Guo, S., Zhao, C., & Tong, M. (2020) A bio-inspired flapping wing rotor of variant frequency driven by ultrasonic motor. *Applied Sciences (Switzerland)*. 10, 1–21. https://doi.org/10.3390/app10010412
29. Chen, S., Guo, S., Xu, H., Ji, B., Tong, M., Wang, L., & Hu, J. (2024) The effect of variable rotary motion of a flapping wing rotor on its aerodynamic performance based on an improved unsteady vortex ring method. *Aerospace Science and Technology*. 145, 108706. https://doi.org/10.1016/j.ast.2023.108706
30. Wang, D., Wu, J., & Zhang, Y. (2013) Aerodynamics on flapping rotary wing in low Reynolds number. *Proceedings of 2013 International Powered Lift Conference*. Los Angeles, Canada, 1–14. https://doi.org/10.2514/6.2013-4382

Click here to access/download
**Supplementary Material**
Author Response Dr Ding2.docx

Declaration of interest

Click here to access/download
**Supplementary Material**
declaration-of-competing-interests.docx

Click here to access/download
**Supplementary Material**
Cover+Letter (1).docx

With Wind video 1

Click here to access/download
**Supplementary Material**
1.mp4

With Wind video 2

Click here to access/download
**Supplementary Material**
2.mp4

With Wind video 3

Click here to access/download
**Supplementary Material**
3.mp4

With Wind video 4

Click here to access/download
**Supplementary Material**
4.mp4

With Wind video 5

Click here to access/download
**Supplementary Material**
5.mp4

No Wind video 1

Click here to access/download
**Supplementary Material**
No Wind 1.mp4

No Wind video 2

Click here to access/download
**Supplementary Material**
No Wind 2.mp4

No Wind video 3

Click here to access/download
**Supplementary Material**
No Wind 3.mp4

No Wind video 4

Click here to access/download
**Supplementary Material**
No Wind 4.mp4

No Wind video 5

Click here to access/download
**Supplementary Material**
No Wind 5.mp4

https://dspace.org/

# Self-locking stability effect induced by downwash flow of the flapping wing rotor

**Chen, Si; Yuan, Lihua; Xiang, Jiawei; He, Yuanyuan; Zhang, Peng ...**

**2025-09**
Springer
https://doi.org/10.1007/s42235-025-00746-0
Chen S, Yuan L, Xiang J, et al., (2025) Self-locking stability effect induced by downwash flow of the flapping wing rotor. Journal of Bionic Engineering, Volume 22, September 2025, pp. 2429-2443

Downloaded from a DSpace repository. https://dspace.org/